university of groningen / faculty of science and engineering

Characterization of the ToF Energy Resolution of an Open Retarding Field Analyzer

Author:
Ennio d'Adamo
s5102200

Supervisor:
prof dr. ir. R. Hoekstra
Daily supervisor:
Lennart Tinge
Second examiner :
Dr. T. Schlathölter

Bachelor's Thesis
To fulfill the requirements for the degree of
Bachelor of Science in Physics
at the University of Groningen

July 6, 2025

Abstract

In the context of ASML's EUV lithography systems, accurate mass and energy measurements of ions are essential for understanding and controlling the effects of hydrogen and tin ions on sensitive optical components. The traditional gridded Retarding Field Analyzer (gRFA) suffers from transmission issues caused by interactions between ions and the grids. To overcome this limitation, an open RFA (oRFA) design is employed in this project. This study focused on the characterization of an open Retarding Field Analyzer operated in ToF mode, with the goal of assessing how the application of retarding voltages affects ToF and energy reconstruction accuracy. Experiments were performed for a monoenergetic He^+ ion beam at 5 keV and 7 keV. The results were compared to simulations and showed good agreement, validating the accuracy of the model in describing ion dynamics within the oRFA. This not only confirms the reliability of the simulations but also opens on the possibility of using them for future design optimization and characterization tasks. Finally, the oRFA introduced increased drift times at higher retarding voltages compared to the gRFA. This trade-off between improved transmission and longer drift times suggests that optimizing the geometry of the oRFA, by adjusting electrode length and spacing, could reduce drift time, affecting the energy resolution. These insights lay the groundwork for further development, particularly in applications requiring the separation of ions by mass or energy in non-monoenergetic beams.

Contents

1 Introduction

Ion detectors play a critical role in various scientific, medical, and industrial applications, underscoring the relevance of this technology. One of their uses is monitoring water purity by detecting harmful ions such as lead or mercury. In medicine, they are used to conduct blood electrolyte tests, measuring sodium, potassium, and chloride levels [1]. In industrial applications, ion detection is equally crucial. ASML uses extreme ultraviolet (EUV) lithography to create nanometer-scale features on chips. EUV light is generated by laser-pulsed tin droplets, producing a plasma that emits both light and high-energy tin ions (Sn^{q+}). To protect the sensitive multilayer mirrors that reflect EUV light, hydrogen gas is introduced. However, EUV radiation also ionizes the hydrogen, creating H^+, H_2^+, and H_3^+ ions. These can have both damaging and beneficial effects on the mirrors, such as causing delamination or assisting with cleaning [2]. Understanding the energy and mass of both tin and hydrogen ions is therefore critical. Time of Flight (ToF) measurements are used in Amsterdam to separate energy and charge of tin (Sn^{q+}) ions, while in Groningen, ToF is used to separate energy and mass of H plasma.

A variety of instruments are used to detect charged particles, including electron multipliers, Faraday cups (FC), photomultiplier conversion diodes, and array detectors [3]. Among these, the retarding field analyzer (RFA) is a particularly versatile device, which combines a Faraday cup with an array of electrodes in front of it. The design that is most commonly found is the gridded RFA (gRFA), where its electrodes have grids disposed to create a localized potential field. This design introduces various drawbacks, such as energy and voltage-dependent transmission, caused by the interaction between ions and the grids. Hence, the design used in this experiment follows the configuration proposed by [4] and consists of four open electrodes. This specific implementation will be referred to as the open RFA (oRFA). A visual depiction of a simulation of the transmission curves, which represent the ions reaching the detector (FC), as a function of the retarding voltage is presented in figure (1), where it is clear why the oRFA configuration needs to be investigated, given its major transmission advantage.

This study focuses on evaluating the performance of the oRFA in time-of-flight mode, specifically in relation to how its energy reconstruction accuracy is affected by varying the voltage on the retarding electrode. Although extensive simulations have been conducted on this topic [5], experimental validation is necessary. To address this, the experimentally observed changes in ToF due to increasing retarding voltages will be compared with simulated predictions. Furthermore, the energy reconstructed by the oRFA will be compared to the known output energy of the ion source at different retarding voltages. This will allow for an assessment of how reconstruction accuracy is influenced as a function of retarding voltage. By analyzing the differences between measured and actual energy values, a detailed characterization of the oRFA's behavior under various configurations will be achieved. In addition, the voltage resolution of the retarding electrode will be described by determining the minimum potential barrier experienced by the ions. All experimental measurements will be carried out using two different ion beam energies of He^+(5 keV and 7 keV).

The research presented in this thesis was conducted in Quantum Interactions and Structural Dynamics (QISD) Group of the University of Groningen. In this group, the interactions between ions and matter are studied. At the ZERNIKELEIF (Zernike Low Energy Ion beam Facility), an ion beam is transported towards one of the setups, called CHEOPS, in which the necessary measurements can be carried.

1.1 Research Questions

How does the application of a retarding potential in an open Retarding Field Analyzer affect the time-of-flight of a monoenergetic ion beam, and how accurately can the resulting energy be reconstructed when compared to simulations and known beam energies.

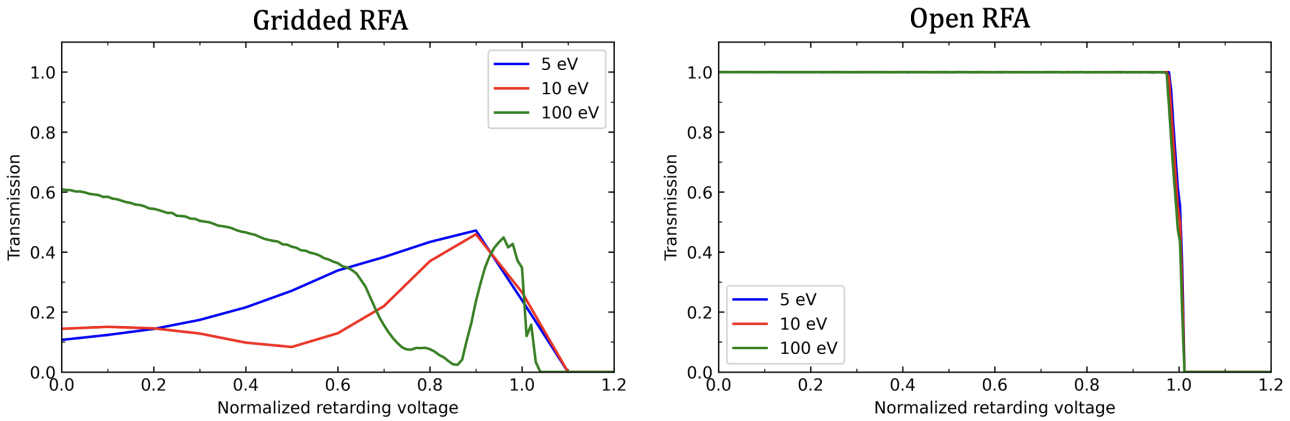

Figure 1: Depiction of the simulated transmission curves versus normalized reading voltages, for both gridded and open RFAs configurations, for three different energies of ion beams.

2 Theory

In this section, the relevant theory behind the working principle of time-of-flight measurement will be explained for both a monoenergetic beam used in this experiment and for a beam composed of an energy spectrum; the latter case will not be reproduced during the experiment, but is what the device will ultimately be used for. In addition, the theoretical characterization of core section of the used retarding filed analyzer will be done.

2.1 Energy Reconstruction via Time of Flight

To reconstruct the energy of ions in a beam, time-of-flight measurements are essential. In this experiment, a monoenergetic ion beam is used, allowing direct comparison between the reconstructed energy and the known energy of the beam. This serves as a means to evaluate the factors influencing the accuracy of energy reconstruction. The principle relies on the relationship between an ion's kinetic energy and the time it takes to travel a known distance. The kinetic energy of an ion is given by (1)

$$E_k = \frac{1}{2}mv^2 \tag{1}$$

Where m is the mass of the ion, and v is its velocity. Although ions may experience changes in velocity throughout the setup, a constant average velocity is assumed for the purpose of this reconstruction [5]. Since velocity is related to the flight time t and path length l by $v = \frac{l}{t}$, the energy equation can be rewritten in terms of quantities that will be experimentally determined:

$$E_k = \frac{l^2 m}{2t^2} \tag{2}$$

With the path length l and ion mass m known, and the flight time t experimentally determined, the kinetic energy can be reconstructed. The flight time is determined by defining an initial time (t_0), typically defined by the moment the ion beam passes through the chopper, and the arrival time (t_r) when the ions reach the Faraday cup (FC). figure (2) shows a visual representation of such a method. By comparing the reconstructed energy to the known energy of the monoenergetic beam, the accuracy of the ToF measurement using the oRFA can be assessed across various retarding voltages and ion energies.

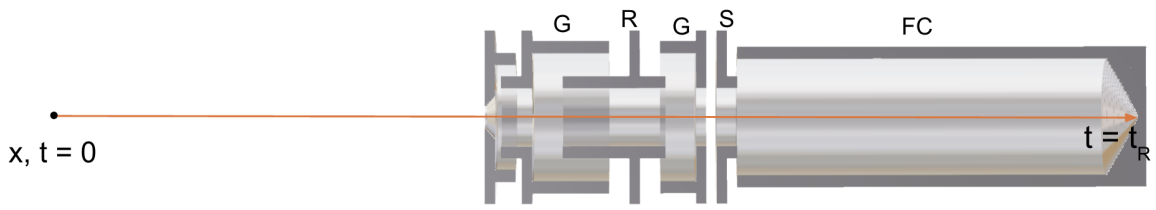

Figure 2: Simplified depiction of the method for ToF measurements, where t_r is the time for energy reconstruction. The specific role of each electrode in the RFA will be explained in Section (3.1)

2.1.1 Energy Reconstruction for a Non-Monoenergetic Beam

The ultimate purpose of the oRFA in Groningen will be to separate hydrogen ions by both mass and energy. Although this functionality is not experimentally explored in the present project, it is important to outline the working principle to fully understand the significance of the device. The objective

is to reconstruct the energy spectrum of the hydrogen (H) plasma using ToF measurements. Figure (3) presents a simulation of a beam composed of hydrogen ions of different masses ($H^+_{1,2,3}$) where the ToF counts are detected. In this image, the voltage values correspond to the potential applied to the retarding electrode, and the black line represents the sum of the individual currents of all three masses, and is similar to what would be observed on an oscilloscope during a measurement. By gradually varying the retarding voltage applied to the electrode, it becomes possible to reconstruct the energy spectrum corresponding to each ion mass, as illustrated on the left of figure (3). Specifically, this can be achieved by subtracting the detected ToF counts between two successive retarding voltage configurations. The resulting difference isolates specific contributions from ions of different masses, leading to a distribution similar to that shown in figure (4). In this figure, the far-right panel shows the outcome of such subtraction, where distinct peaks appear. These peaks arise due to differences in ion mass: H^+ ions, having the lowest mass, arrive earlier than H^+_2, which in turn are faster than H^+_3. Consequently, the peaks can be assigned to specific ion species.
In real experimental conditions, these peaks are expected to broaden and shift towards higher time of flight. and partially overlap if the effect of the retarding potential on the ToF is large enough, complicating the mass and energy separation process. Therefore, characterizing the oRFA's performance in ToF mode is critical for its future applications.

2.2 Potential Resolution

A central objective of this project is to examine how the time-of-flight of a monoenergetic ion beam changes when a retarding voltage is applied to the Retarding Field Analyzer (RFA), and how this in turn affects the accuracy of energy reconstruction. The voltage applied to the retarding electrode introduces a potential barrier that slows down ions passing through it, thereby increasing their arrival time t_r. As a result, an increase in ToF is expected, potentially reducing the accuracy of energy reconstruction. One of the goals of this work is to quantify this effect. A detailed explanation of the retarding electrode's operation is provided in Section (3.1). The retarding electrode used in this setup has a radius of 2.5 mm and a length of 10 mm. Simulations were used to determine how the electric potential scales at the center of the electrode. This scaling is defined by the k-value (k_{val}), which depends on the electrode's geometry, its distance from the grounded electrode, and the voltage applied to the suppressor. In this study, the suppressor is not used and grounded, resulting in a $k_{val} = 0.99481$. This implies that the ions passing through the retarding electrode experience a minimum potential equal to 99.48% of the applied voltage. A visual representation of the potential distribution within the retarding electrode is shown in figure (5).

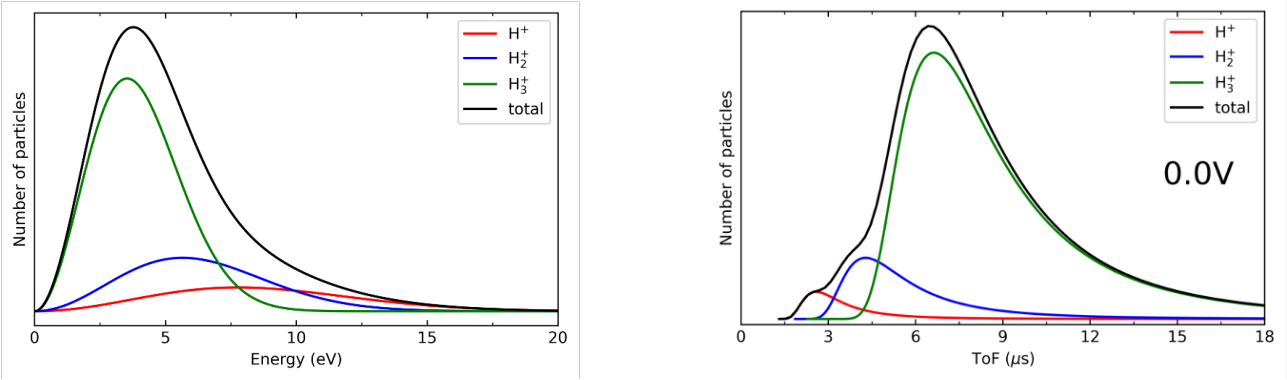

Figure 3: Simulated results illustrating how ToF measurements can be used to reconstruct the energy distribution of a non-monoenergetic hydrogen ion beam. The left plot shows the simulated energy distribution used for input in ToF simulations, while the right plot displays the ToF distributions for each ion species.

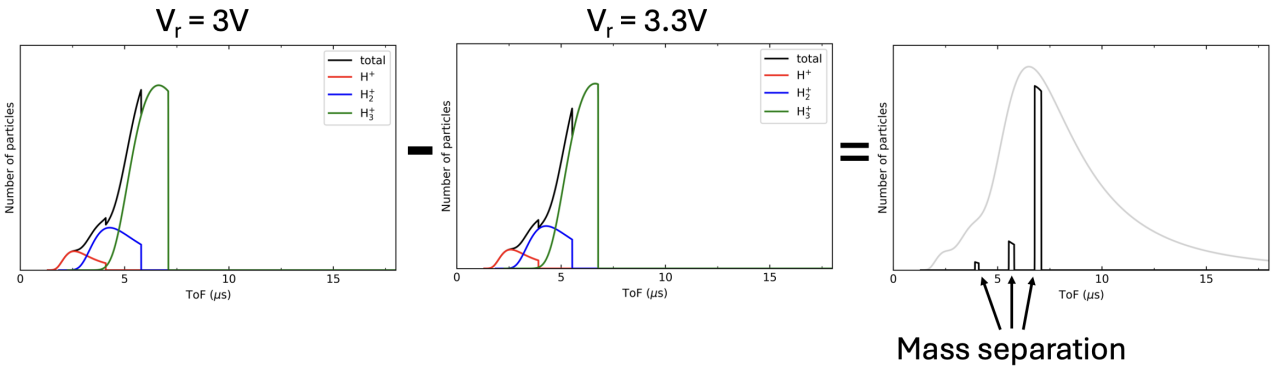

Figure 4: Simulation illustrating mass separation of a non-monoenergetic ion beam. By subtracting ToF counts at successive retarding voltages, distinct peaks emerge, each corresponding to a different ion mass. Lighter ions have shorter ToF, allowing mass identification.

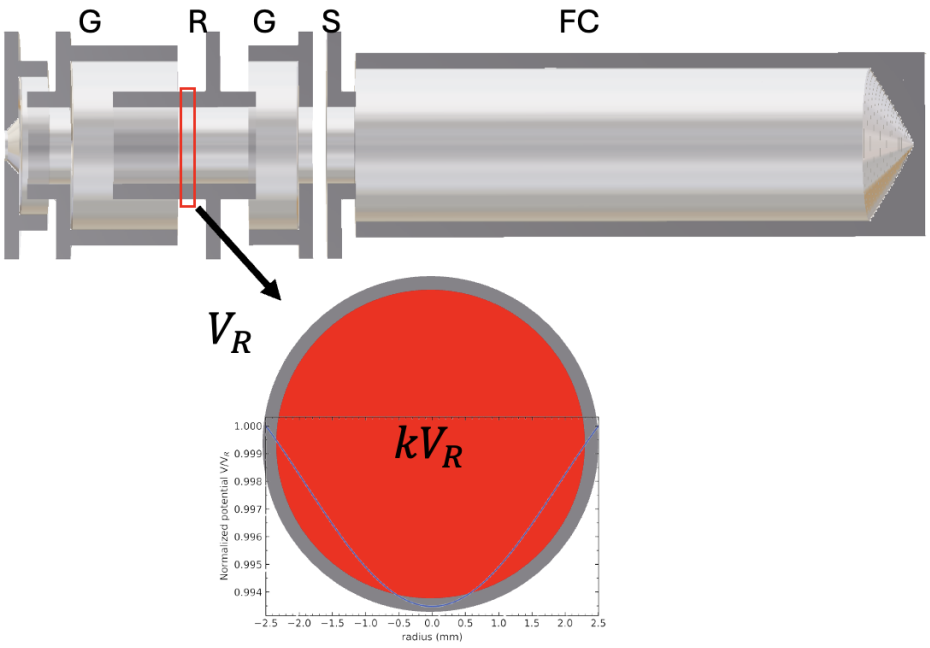

Figure 5: Potential distribution across a section of the retarding electrode. The plot shows how the potential experienced by the ions decreases toward the center of the electrode, reaching a minimum value equal to the applied voltage multiplied by the k-value.

2.3 Simulation background

To understand how the oRFA influences the time-of-flight of ions, a numerical simulation was developed. This simulation models the effect of a spatially varying retarding potential on the ion beam passing through the point (0,0) in figure (6) and calculates the extra ToF introduced by the retarding electrode, based on ion energy and applied retarding voltage. The simulation operates by tracking ions as they traverse the oRFA along the longitudinal axis. At each small spatial step along the beam path, the local energy of the ion is updated based on the instantaneous retarding potential experienced at that position. This local potential is derived from Simion simulations corresponding to the geometry of the retarding electrode. Additionally, to find the effect at different retarding voltages, the potential map is scaled depending on the desired voltage.
As the ion progresses through the device, the time required to travel through each segment is computed from the ion's instantaneous velocity subtracted with the time it would have traveled without the effect of the retarding potential. By summing the time increments across the entire retarding region, the total extra ToF through the oRFA is obtained. The process is repeated for different retarding voltages, such that the effect is found as a function retarding potential. The result of this simulation will be compared to the experimental data to determine its validity. Additionally, simulations are going to be useful to understand the performance limitations introduced by the geometry and design of the RFA.

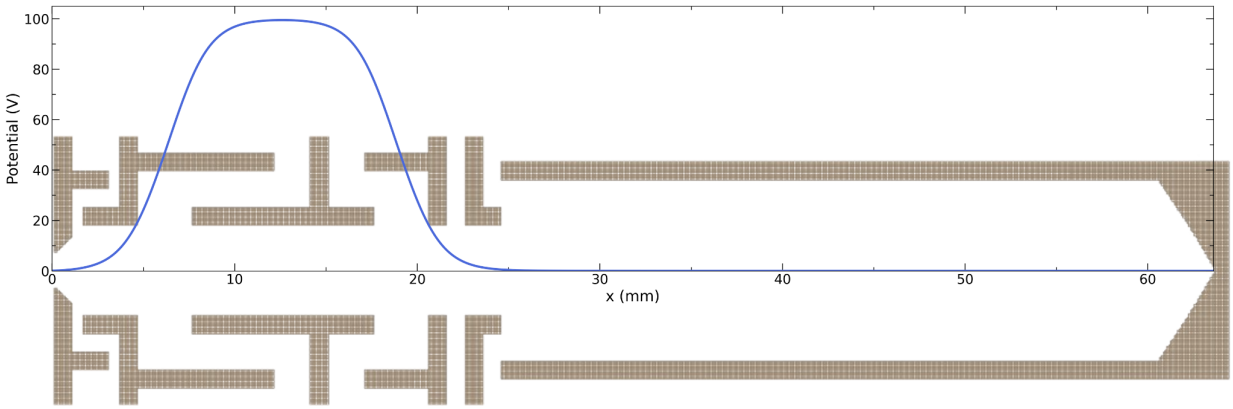

Figure 6: Simulation of the oRFA geometry with the corresponding retarding potential distribution overlaid. This environment provides the spatial profile of the chosen retarding potential used to observe the ion ToF through the device.

3 Experimental Setup

To investigate energy reconstruction using time-of-flight measurements for a monoenergetic ion beam, a standalone setup was initially built. However, its performance proved insufficient for collecting clear data. Consequently, the experiment was conducted using CHEOPS, a setup specifically designed for such operations and capable of achieving relatively high ion beam currents produced in the ZERNIKE-LEIF. Both setups will be characterized in the following sections, along with the oRFA.

3.1 oRFA

The retarding field analyzer detector employed during this experiment uses a series of cylindrical electrodes to introduce a high-pass energy filter. The device is illustrated in figure (7). The detector is composed of a series of components through which ions travel from left to right in figure (7). Each electrode serves a specific purpose to ensure proper operation. These electrodes, excluding the grounded ones, can be independently biased for precise control. The role of the devices will be explained in the order the ions encounter them.

Grounded Electrodes:
The first of the two grounded electrodes prevents the field from escaping the apparatus. This containment prevents incoming ion beams from interacting with stray electric fields before entering the detector. The second electrode makes sure that the suppressor and the retarding electrode do not interact, since voltages of opposite magnitude are applied which could compromise the distribution and the strength of the potential.

Retarding Electrode:
A positive voltage, V_{ret}, is applied to this electrode to create an electric field that selectively allows ions with sufficient kinetic energy to pass while blocking others, enabling the detection of particles with a specific minimum energy. The energy threshold is described by:

$$E > \frac{V_{ret}}{q}, \tag{3}$$

where E is the kinetic energy of the ion in eV, V_{ret} is the applied voltage and q is the charge of the ion. The effect of applying a voltage to this electrode during ToF measurements will be assessed for energy resolution. As described in 2.2, the potential distribution is heavily geometry dependent.

Suppressor Electrode:
This electrode ensures that the detected current corresponds only to the ion current. The suppressor electrode is negatively biased to prevent secondary electrons from escaping the Faraday cup when they interact with the latter. It also ensures that electrons produced by the ion impact anywhere in the RFA before the suppressor do not enter the FC [6]. Additionally, in a plasma environment, the suppressor electrode prevents plasma-induced electrons from entering the Faraday cup.

Faraday Cup:
At the Faraday cup, the charge deposited by the ion beam colliding with it is measured. A typical Faraday cup is a cylindrical, shielded container into which the charged particle will interact, and the charge induced on the inner electrode of the cup is determined by an electrometer [7]. When the ions strike inside the cup (labeled FC in figure 7), the amount of charge induced on this surface is

determined by the current needed by an external circuit to neutralize such surface, effectively allowing for measurement of the ion beam current.

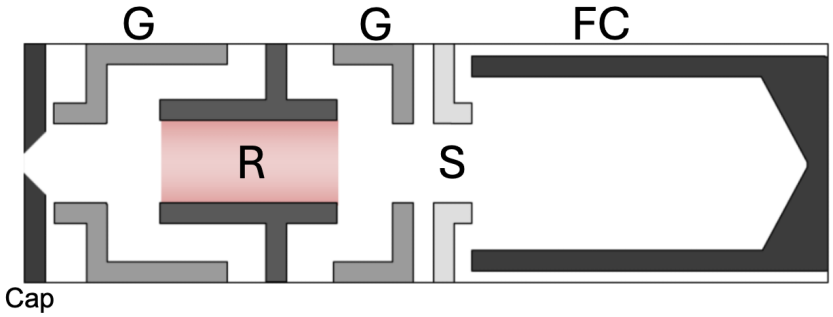

Figure 7: Depicts the schematic of an oRFA, with (G) grounded electrodes, (R) retarding electrode, (S) suppressor electrode and the Faraday cup (FC). Image adapted from [8].

3.2 Stand Alone Setup

Before performing measurements on CHEOPS, an attempt was made to build a standalone setup. The main components and their functions are described in the order in which the ions interact with them. These components are also key elements later integrated into CHEOPS. The layout of the setup is illustrated in figure (8), where the ion beam travels from right to left. The setup began with an ion gun capable of producing low-energy ion beams, with a maximum energy of 700 eV. This low energy also contributed to the reduced ion current observed at the FC. The RIBER ion gun included two lenses for beam focusing and an extractor to extract ions generated inside the ion source. Following the ion gun, the beam passed through the chopper-sweeper system, a critical component for defining the start time t_0 of the measurement. This timing is essential for accurate time-of-flight analysis. The chopper, shown in figure (8), consists of two pairs of plates with opposite voltages applied. These voltages cause the beam to deflect, preventing it from passing through the diaphragm located after the plates. When the polarity is rapidly switched (with a frequency of 10 kHz), the beam is allowed to pass briefly; this instant defines t_0. In this experiment, only one pair of plates was used; therefore, the device will hereafter be referred to as the Chopper. Subsequently, the ion beam enters the Retarding Field Analyzer, described in detail in Section (3.1). The current measured at the FC reached a maximum of approximately 3 nA, which was insufficient for obtaining reliable data. As a result, a transition to a more advanced setup (CHEOPS) became necessary. A current-to-voltage transimpedance amplifier [9] was employed to enable signal detection. This device is connected to the 50 Ω input of the oscilloscope. The amplifier outputs 25 kV per Amp, hence amplifying one μA into 25 mV. This signal amplification comes with the cost of introducing high noise in the system, due to the amplifier picking up signals coming from the rest of the setup. By grounding the suppressor electrode of the RFA, this noise could be minimized. In order to retrieve clear data on the oscilloscope in averaging mode, a minimum value of approximately 60 nA is needed to reach the FC. This same amplifier was later used in the CHEOPS system to perform the same function. In figure (9), an image of the oscilloscope display can be seen when no ion current is sent into the oRFA. The green line is the block pulse that activates the chopping at the falling edge, while the yellow line corresponds to the output of the FC. Vacuum conditions, essential for operating an ion beam setup, were achieved using turbo and scroll pumps. The pressure reached around 10^{-6} mBar during operation.

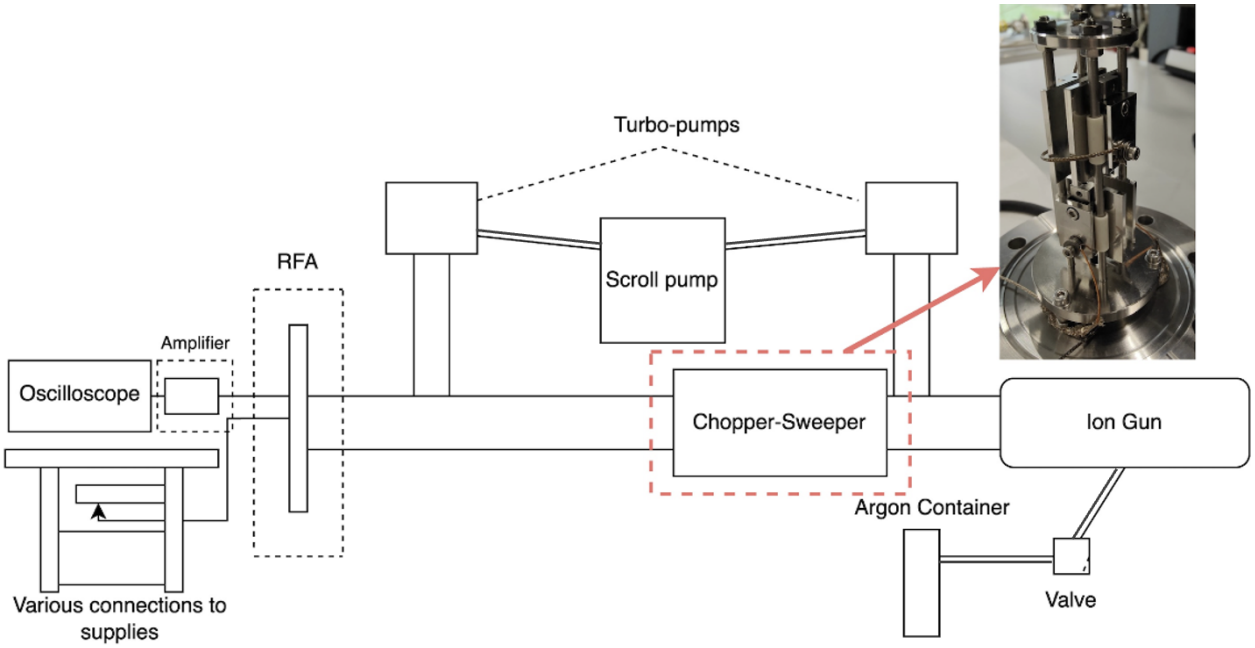

Figure 8: Depicts a schematization of the stand-alone setup that was built before switching to CHEOPS, the chopper sweeper is also visible outside of the setup to have a better representation of this fundamental piece.

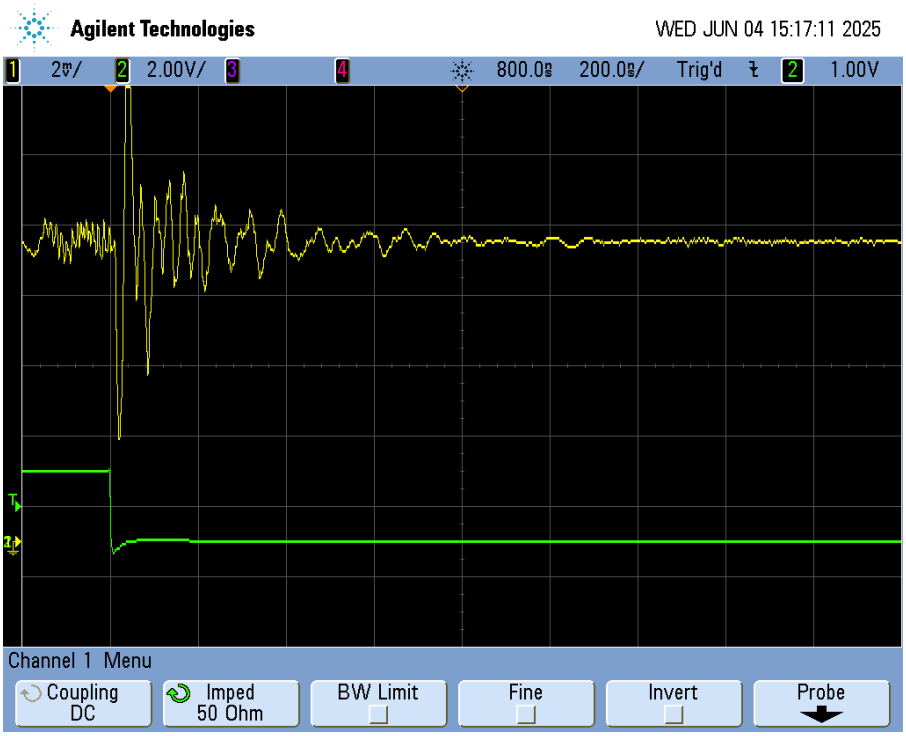

Figure 9: A depiction of the display of the oscilloscope connected to the pulse generator and the amplifier when no ion current is generated. The yellow line corresponds to the amplified noise signal from the FC. The oscilloscope is triggered on the falling edge of the green signal from the pulse generator, indicating the moment the ion beam is chopped (green).

3.3 Zernike Low Energy Ion Facility

3.3.1 Ion Production

In ZERNIKELEIF, an electron cyclotron resonance ion source (ECRIS) is used for the creation of a plasma, consisting of different ions. A depiction of the set-up is visualized in figure (10). Different gases can be added to the ion source from which a plasma is produced. These gases are usually noble gases; during this project, Helium was used since the current output was the highest. When the gases are introduced into the chamber, a strong permanent magnet causes free electrons to perform a cyclotron motion. In addition, a radio frequency (RF) resonant with the frequency of the cyclotron motion accelerates the electrons so that they have enough energy to ionize the gas [8]. This creates a plasma with ions of different charge states. The energy that the ions will possess is dictated by $E_{ion} = q(V_{ECR} + V_{plasma})$ where V_{ECR} is a positive potential at which the source is set. Normally, the value of the plasma potential (V_{plasma}) is negligible compared to the source voltage [8]. Hence, the energy of the ion beam is mainly determined by the source voltage and the ion's intrinsic charge (q).

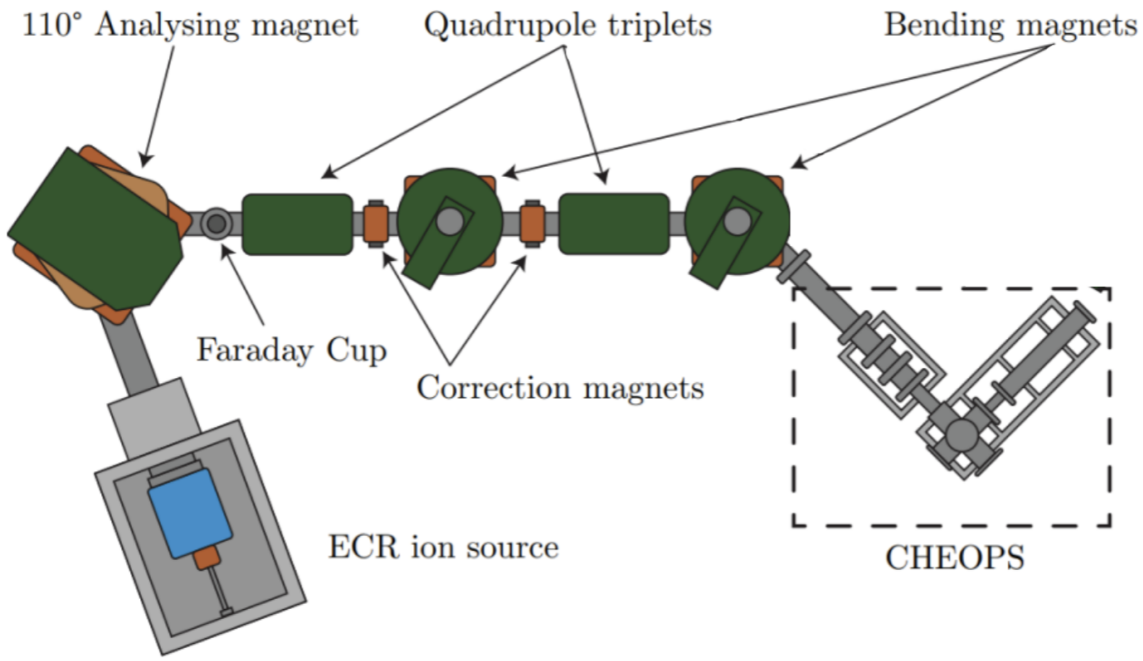

Figure 10: Depicts the full setup used to carry out the experiment. A schematization of the ECR ion source can be visualized, with the various bending magnets, correction magnets, and quadrupole triplets. The beam's final destination (CHEOPS) can also be visualized. Image adapted from [10].

3.3.2 Transport

After being produced, the beam will be transported towards CHEOPS. Transportation is facilitated by two triplet quadruple focusing magnets and two correction magnets, figure (10). The triplet quadruple magnets focus the ion beam, "squeezing" it. The two correction magnets are placed some distance apart and allow for a correction of the trajectory of the ion beam. The correction magnets can bend the ion beam slightly in the vertical and horizontal direction. The beam will then encounter a 45° bending magnet to get introduced into the CHEOPS setup.

3.3.3 CHEOPS

The abbreviation CHEOPS stands for Charge Exchange Observed by Particle Spectroscopy. The setup is mainly used to study ion-gas interactions. However, it is also possible to perform ToF experiments without introducing gas interactions to it. A schematic of CHEOPS setup can be visualized in figure (11), where the beam goes through an einzel lens, used to focus the beam, after which the chopper is encountered, its purpose is the same as illustrated in the stand-alone setup. Before reaching the RFA, the beam goes through a set of deceleration lenses, which in this case can have a negative potential to them, effectively accelerating the beam. Additionally, these lenses further focus the beam. The deceleration lenses significantly increase the current reaching the FC, potentially even by a factor of 10. The beam will then go through the collision chamber, where a gas capillary and the extraction plates are present; for the purpose of this project, neither are in use. Finally, the beam reaches the oRFA. Once the ions interact with the FC, the current signal will go through the amplifier in order to gather voltage values on the oscilloscope.

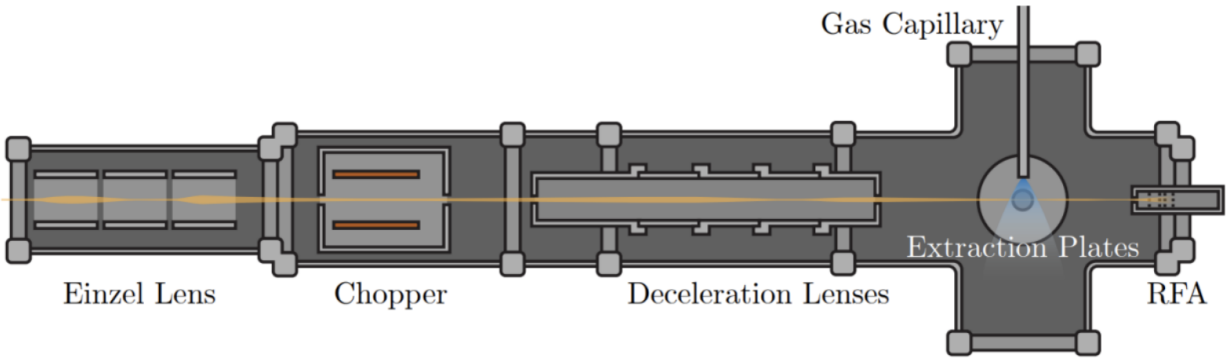

Figure 11: Schematic overview of CHEOPS [10] with all the components that the ion beam will encounter from left (entrance) to right (end of setup). The ion beam current is measured by the open retarding field analyser. The Gas capillary and extraction plates are not in use during the project.

4 Results

In this section, the experimental results are presented and analyzed. The differences in ion arrival times (ΔToF) under varying retarding electrode potentials are compared to simulation predictions. These comparisons are made for both active and inactive deceleration lens configurations, and for both ion beam energies. Finally, the reconstructed energies are compared to the actual beam energies in order to assess the energy resolution of the open Retarding Field Analyzer.

4.1 Data Characterization

4.1.1 He^+ 7 keV

To evaluate the effect of the retarding potential on time-of-flight, the arrival time at 0 V on the retarding electrode is used as the reference point. All subsequent ToF values are compared against this baseline to quantify the shifts induced by applied retarding voltages. For the configuration with active deceleration lenses, 48 data points were collected, with current recorded at FC of 1.2 μA. The retarding voltage was incrementally increased up to a maximum of 7015 V. The fact that ions are still detectable over 7 keV can be explained by considering the potential k value at the center of the electrode; hence, ions passing through the center will experience a slightly lower potential. Beyond 7015 V, the detected current becomes incoherent and unstable, as the potential barrier exceeds the energy of most ions, the signal decreases below noise levels, making it impossible to identify a consistent ToF peak. This behavior is illustrated in figure (12). In the case where the deceleration lenses were inactive, 42 data points were analyzed with current at the FC of 140 nA. The maximum voltage that still produced coherent current readings at the FC was 6970 V. Beyond this point, the number of ions capable of overcoming the potential barrier dropped below the detection threshold. This is consistent with theoretical expectations from equation (3), which predicts that ions with 7000 eV kinetic energy should be fully stopped by a 7000 V retarding potential in the absence of any pre acceleration. figure (13) shows a comparison between the voltage readings at 0 V and 7060 V, where the ToF peak is no longer observable due to the absence of transmitted ions.

4.1.2 He^+ 5 keV

For the ion beam energy of 5 keV, the configuration with active deceleration lenses yielded a measurable current of 520 nA at the Faraday Cup when no retarding potential was applied. A total of 46 usable data points were collected as the retarding voltage was gradually increased up to 5000 V. Beyond this point, the current dropped to zero, indicating that the retarding potential repelled enough ions that the signal dropped below the detection limit. In contrast, the configuration without active deceleration lenses resulted in a significantly lower current of 72 nA at the FC. This value was insufficient to perform reliable measurements across a range of retarding voltages, as signal coherence would degrade too quickly. Consequently, only the data point at 0 V on the retarding electrode was acquired in this configuration, and it was used solely for energy reconstruction purposes. The oscilloscope readings for specific retarding voltages are depicted in appendix (22, 23).

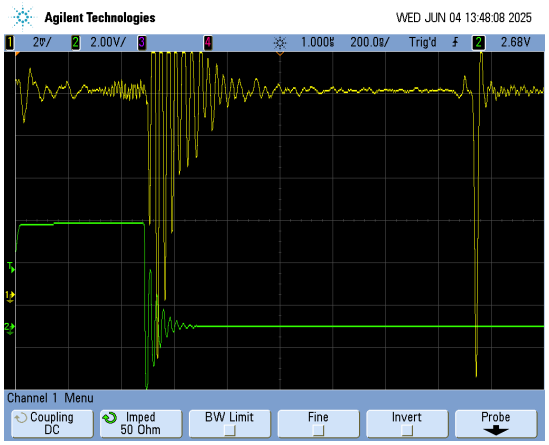

(a) Depiction of the voltage produced by the ions hitting the FC (far right dip), for 0 V applied to the retarding electrode.

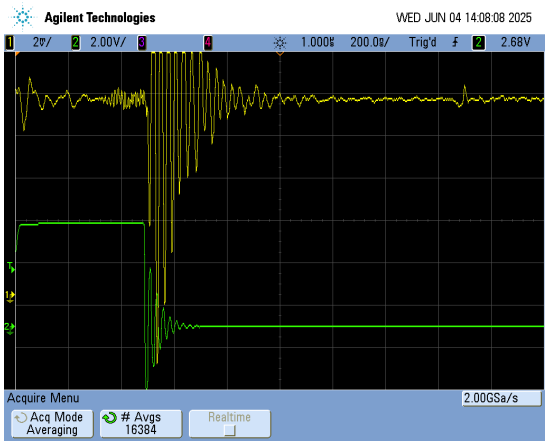

(b) Depiction of the voltage produced by the ions hitting the FC, for 7060 V applied to the retarding electrode.

Figure 12: Depiction of the signal from the transimpedance amplifier at the oscilloscope (yellow line), when the deceleration lenses are active. Where the dip on the right side represents the current generated by the ions. For 2 values of retarding voltage, 0 V and 7060 V. For the latter voltage, no dip is recognizable just after the noise region.

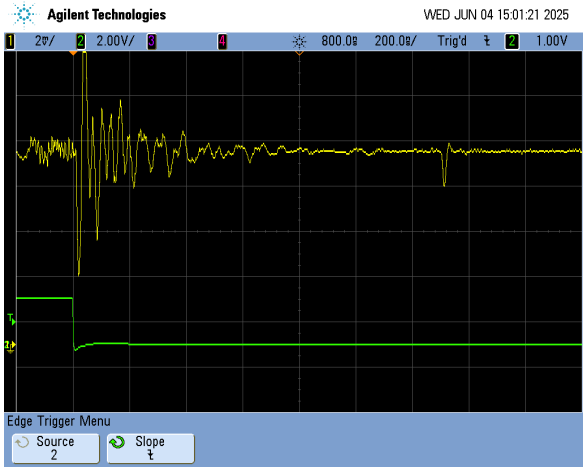

(a) Depiction of the voltage produced by the ions hitting the FC (dip on the right), for 0 V applied on the retarding electrode.

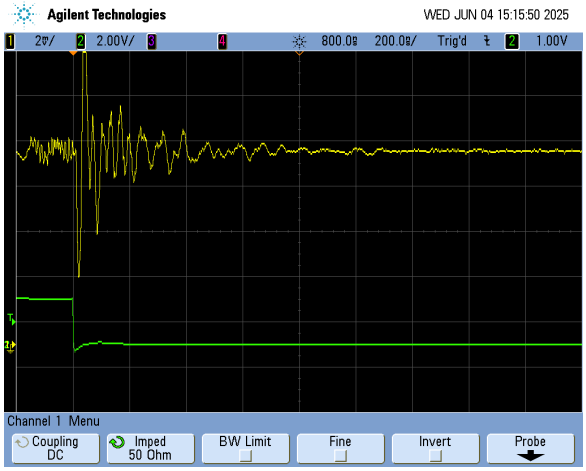

(b) Depiction of the voltage produced by the ions hitting the FC, for 7060 V applied on the retarding electrode.

Figure 13: Depiction of the voltage at the oscilloscope when the deceleration lenses are inactive (yellow line), where the dip on the right side represents the current generated by the ions. For 2 values of retarding voltage, 0 V and 7060 V. For the latter voltage, no dip is visible since the ion current has dropped below the detection limit of the amplifier.

4.2 ToF Difference of 7 keV and 5 keV

The relationship between retarding voltage and ToF reveals important physical behavior of the system. As V_r approaches the beam energy E_0, the ToF increases asymptotically, theoretically diverging to infinity when the retarding potential matches the ion energy. This behavior stems from the fundamental dynamics of charged particles in retarding potentials, as the potential barrier approaches the particle's kinetic energy, its velocity through the measurement region diminishes, leading to longer drift times. However, several experimental factors limit the observation of this ideal asymptotic behavior. The finite resolution of the voltage supply prevents operation in increasingly small steps. More significantly, as ions approach this condition, their signal becomes increasingly delayed and attenuated, eventually falling below the detection threshold of our amplification system.
For each retarding voltage value, the time-of-flight is determined by subtracting the time corresponding to the chopper trigger t_0 (represented by the descending edge of the block pulse, shown in green) from the time of the voltage dip associated with ion arrival (indicated by the yellow line), as illustrated in figures (12, 13), this dip is defined from the position of the lowest voltage value.
Using the ToF measured at 0 V on the retarding electrode as a baseline, the ToF differences (ΔToF) for increasing retarding voltages are plotted in figures (14, 15, 16) for all three configurations, with and without active deceleration lenses. The 5 keV beam with inactive deceleration lenses is not represented since not enough data points could be gathered for this specific comparison. The resulting plots show good agreement with simulated expectations: in both cases, ToF increases as the retarding voltage increases, consistent with the ions slowing down due to the potential barrier. The configuration shown in figure (15) achieves higher voltages measurements due to the presence of the deceleration lenses, which allow for better focusing increasing the signal, making the signal detectable over the noise range for higher values of retarding voltages. Overall, both configurations demonstrate reliable and promising behavior in line with theoretical predictions.

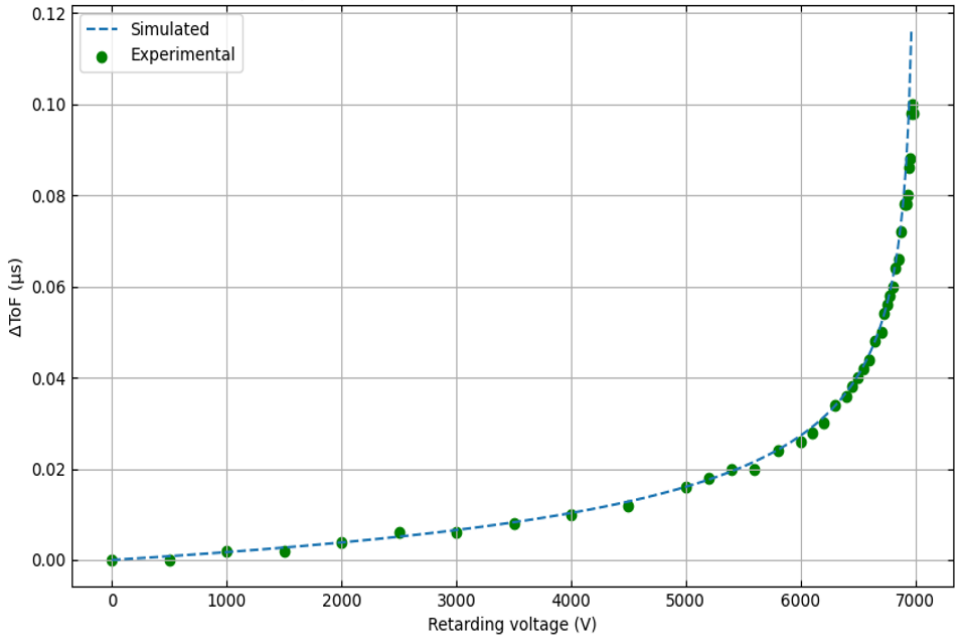

Figure 14: Depiction of the ToF difference versus retarding voltage, and simulated ΔToF, for the configuration that does not use deceleration lenses for 7 keV He^+ ions.

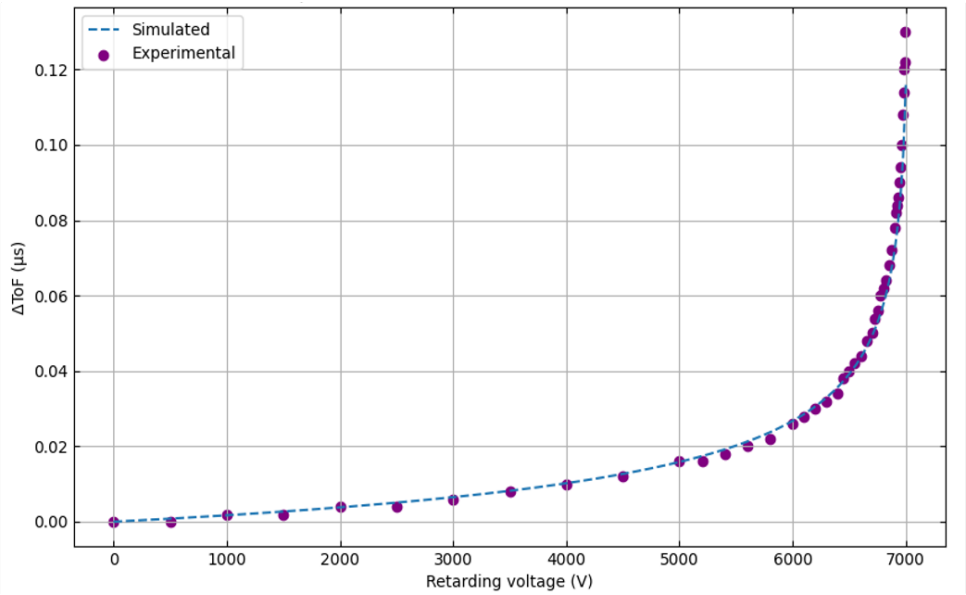

Figure 15: Depiction of the ToF difference versus retarding voltage, and Simulated ΔToF, for the configuration that has active deceleration lenses for 7 keV He^+ ions.

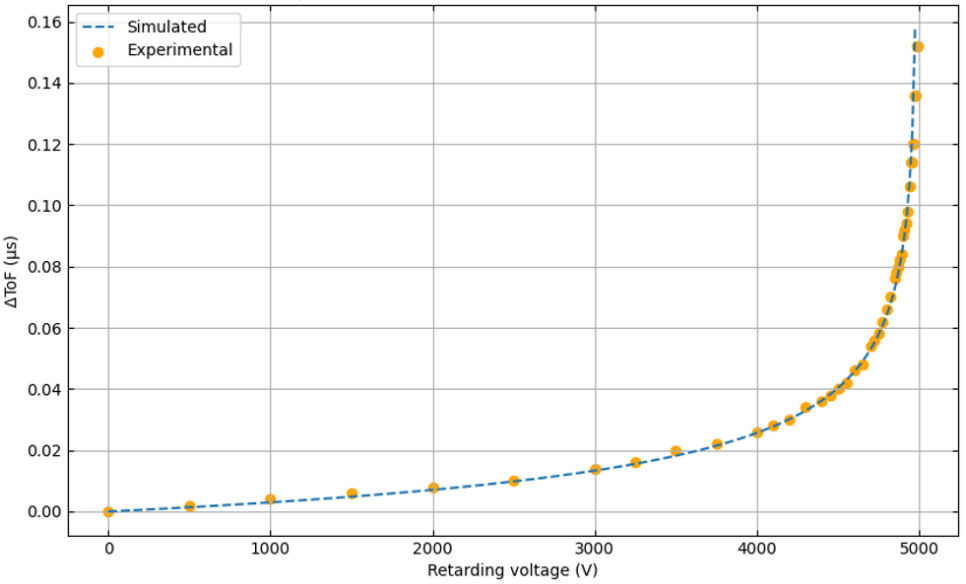

Figure 16: Depiction of the ToF difference versus retarding voltage, and Simulated ΔToF, for the configuration deceleration lenses for 5 keV He^+ ions.

4.3 Correction for deceleration lenses & energy reconstruction

The use of deceleration lenses played a key role in this project by significantly increasing the current output of the setup. However, this enhancement came with a drawback: the lenses reduced the ions' time-of-flight, thereby affecting the accuracy of energy reconstruction. Given that measurements were performed with and without a voltage applied to the lenses, the effect on the ToF could be found. To address this, a correction was introduced to account for the ToF reduction caused by the lenses. This correction was defined as the difference in ToF between configurations with and without active deceleration lenses at 0 V retarding voltage. The measured differences were $\mathrm{ToF}_{change(7\ \mathrm{keV})} = 60$ ns and $\mathrm{ToF}_{change(5\ \mathrm{keV})} = 64$ ns.

Following the ToF measurements, the length of the setup can be calculated and used for energy reconstruction via equation (2). A retarding voltage sweep was first performed, and by identifying the maximum retarding voltage V_r at which ions still reached the FC, an estimate of the actual energy of the ion beam was obtained. This procedure was carried out for both 7 keV and 5 keV beams. For the former, the maximum V_r was 7020 V, and for the latter, 5011 V. While the source sets the nominal ion energy, slight variations are still present due to the beam formation process. The 110-degree bending magnet, located downstream of the source, serves as both a mass-to-charge selector and an energy filter. It reduces the beam's energy spread to below 1%, ensuring a nearly monoenergetic distribution. However, the residual spread means the actual energy of the beam is effectively an average over a narrow distribution, which may introduce small systematic deviations in the energy estimate, and consequently, in the derived setup length. The two V_r values correspond to the applied voltage on the retarding electrode. However, as explained in Section 2.2, the ions experience the minimum potential at the center of the electrode. Thus, the effective potential, representing the beam energy, is calculated by multiplying V_r by the k-value. Using the ToF from the configuration with inactive deceleration lenses and 0 V on the retarding electrode, the length l of the setup was calculated using the expression:

$$l = \sqrt{\frac{2V_r k_{val} t^2}{m}} \tag{4}$$

Slightly different values were obtained for the 5 keV and 7 keV cases, and the final result calculated here corresponds to their average. The length is reported as $l = 0.763$ m. This length was then used in equation (2) to reconstruct the ion energy based on the measured ToF. In figure (17), where the deceleration lenses are inactive, the trend of reconstructed energy versus retarding voltage can be observed. The behavior matches the simulated expectations, showing a decreasing accuracy as the retarding voltage increases. This is attributed to the extra drift time introduced by the retarding potential.

For the 7 keV beam with active deceleration lenses accounted for in figure 18, the same trend is followed, providing consistent results, indicating that this correction applied to this configuration is effective. A similar plot for the 5 keV beam with inactive deceleration lenses could not be produced due to insufficient data points. However, the case with active lenses is presented in the Appendix (24), where again their action is already accounted for.

The reconstructed energy values at 0 V retarding voltage with inactive deceleration lenses provide an important consistency check between different measurement methods. The results, $E_{\mathrm{Rec,7\ keV}} = 6990.24$ eV and $E_{\mathrm{Rec,5\ keV}} = 4984.98$ eV, show close agreement with the energies determined from the voltage sweep measurements (7020 V and 5011 V respectively). This correspondence validates our experimental approach.

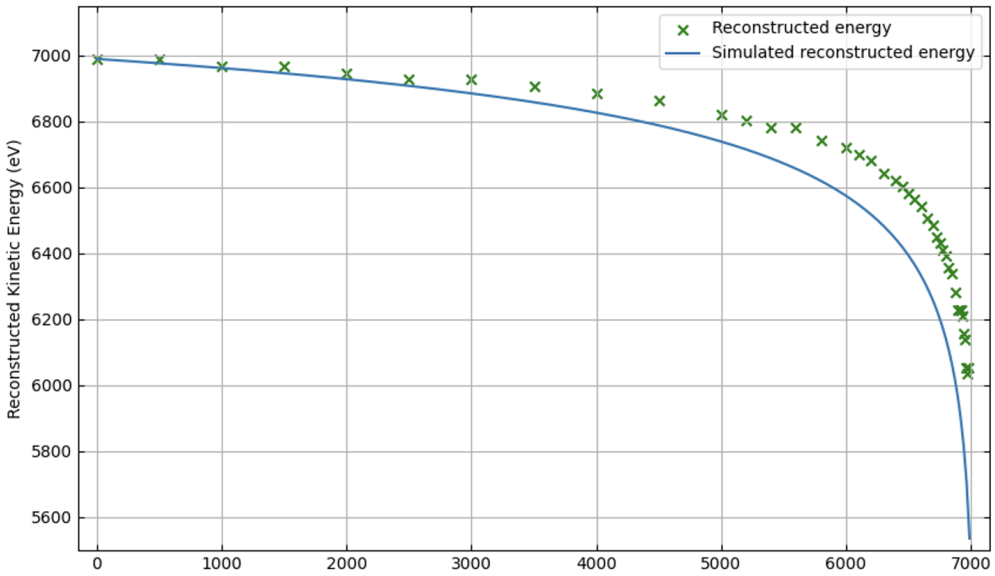

Figure 17: Depiction of the reconstructed energy for a range of retarding voltages, compared to the simulation expectation, for the helium beam with 7 keV energy, having inactive deceleration lenses.

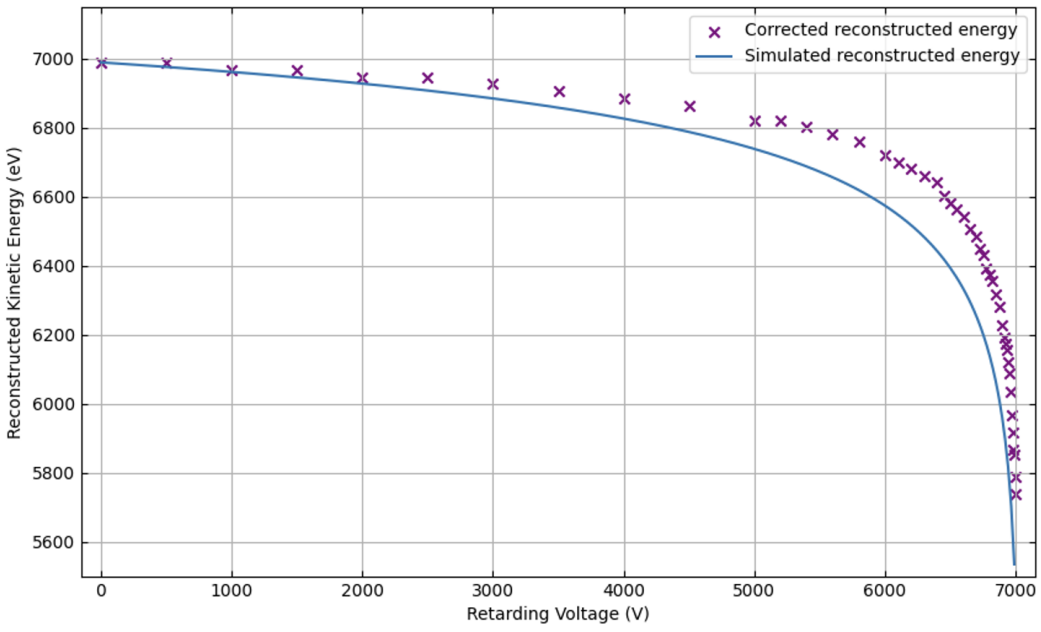

Figure 18: Depiction of the reconstructed energy for a range of retarding voltages, compared to the simulation expectation, for the He^+ beam with 7 keV energy having active deceleration lenses.

To evaluate the effectiveness of this correction, a plot of the ratio between the reconstructed energy and the actual beam energy (E_R/E_0) versus the ratio of the beam energy to the retarding voltage (V_r/E_0) was produced and compared with simulation results. figure (19) shows this ratio for the case without deceleration lenses, giving the expected normalization of figure (17). Minor deviations at higher retarding voltages are attributed to unaccounted lensing effects and increased ion beam disorder near the potential barrier.

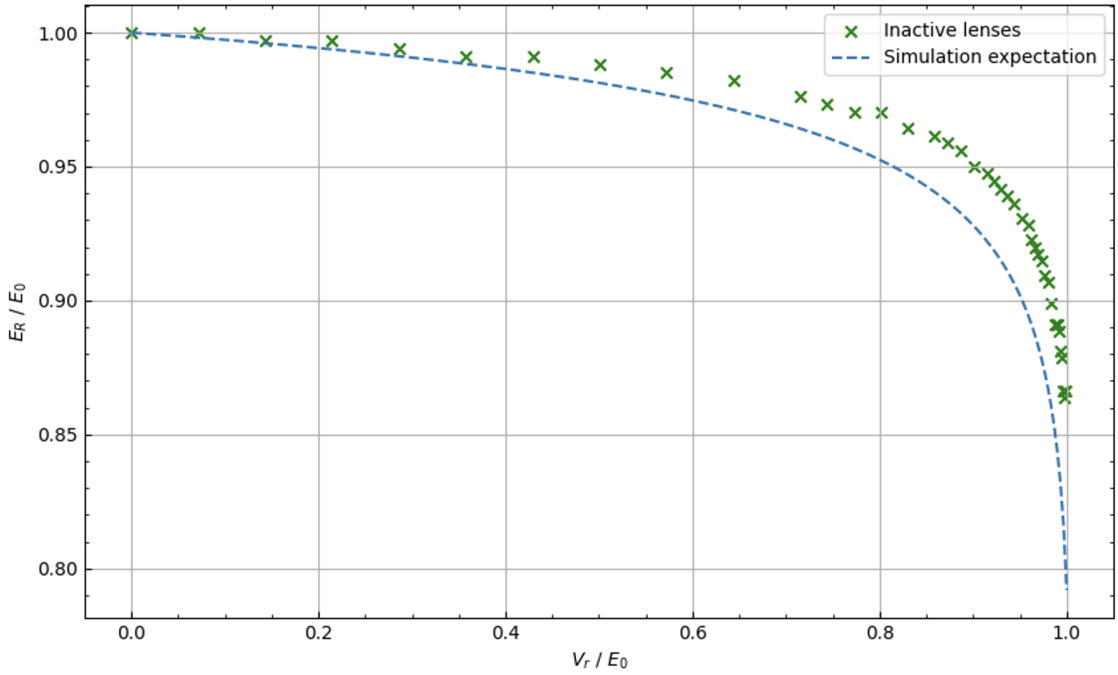

Figure 19: Depiction of the trend followed by the ion beam reconstructed energy, compared to the simulation expectation, when the deceleration lenses are inactive.

Regarding the 5 keV instance, the specific plot of the E_R/E_0 could not be made from the configuration without deceleration lenses. However the ToF value individuated with no retarding potential is used to determine the correction for this specific configuration. figure (20) displays data of E_R/E_0 vs E_0/Vr for both 5 and 7 keV cases of He^+ energies, when the lenses are active. For the case of the 7 keV beam, the ToF values have been corrected by applying the previously determined ToF_{change}. The same procedure is performed on the 5 keV beam; the action of the deceleration lenses can be accounted for by adding the ToF change, which in this case is 64 ns, and is higher than for the 7 keV. This difference arises because while both ion energies receive the same absolute energy increase from the lenses, the relative change is greater for lower energy ions. Both these configurations follow the same trend, showing that this behavior is independent of energy, suggesting a high degree of confidence in the results and measurements.

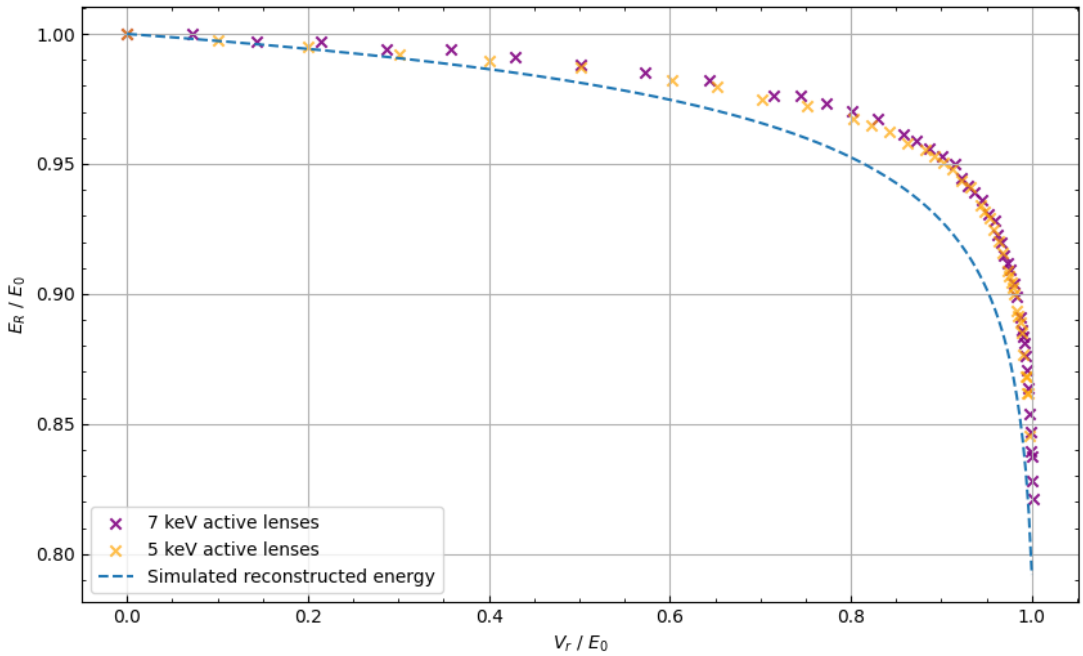

Figure 20: Depiction of the trend that both normalized reconstructed energies for 7 keV and 5 keV follow, after being corrected for the active deceleration lenses. The curves show an energy-independent behavior.

4.4 Simulation comparison

The experimental results demonstrate strong agreement with the simulations, confirming that the model accurately captures the physical behavior of ions within the oRFA. This highlights the utility of the simulation framework for characterizing different RFA geometries and predicting ion drift times across various configurations.
figure (21) shows the simulated drift times as a function of retarding voltage for the gridded RFA, widely in use for ion diagnostics. As explained in section (1), this configuration introduces additional complexities such as electrostatic lensing effects, ion–grid interactions, and makes the transmission unstable, compared to the open RFA. These limitations motivate the investigation and potential replacement of the gRFA with the oRFA, provided its performance can be sufficiently understood and optimized. To that end, figure (21) compares two different oRFA geometries. The wider distribution of drift times observed for the oRFA relative to the gRFA can be attributed to the longer interaction of ions with the extended retarding field. However, modifying the oRFA design, such as by shortening the retarding electrode, which narrows the potential distribution in the RFA, reducing the drift time spread. This comes at the expense of a slight decrease in energy resolution, as evidenced by the inability to fully stop 7 keV ions due to a lower effective potential at the center of the electrode.
These findings suggest that the geometry of the oRFA can be tuned to minimize drift time while maintaining acceptable energy resolution. Furthermore, extending the total ion flight path would reduce the relative influence of the drift zone on the overall time-of-flight, providing another route for performance optimization.

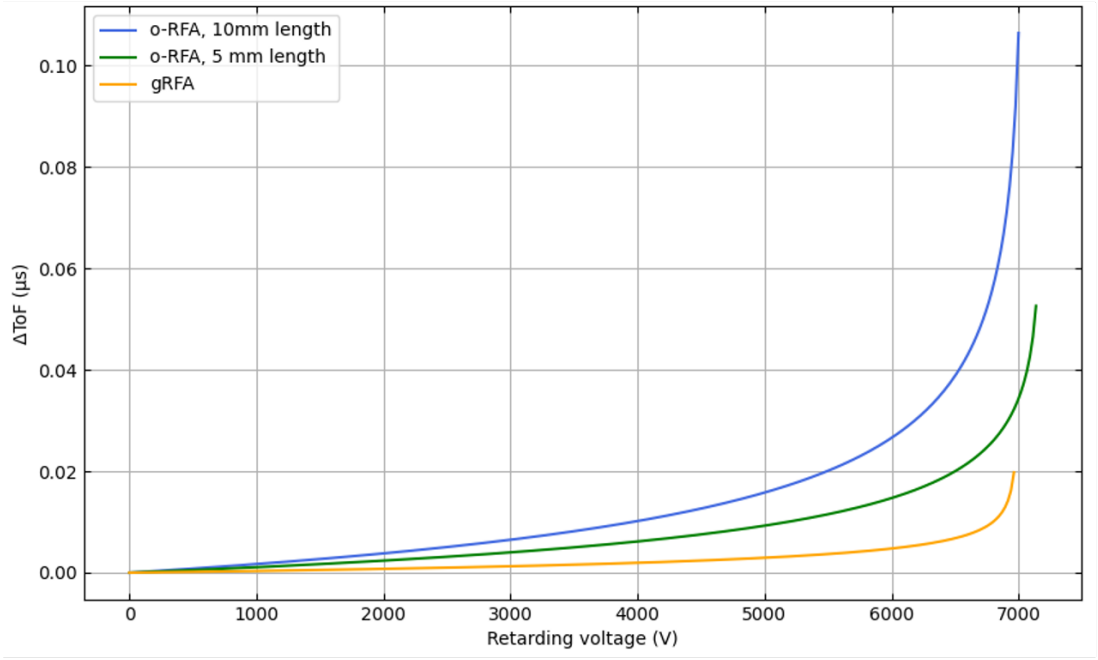

Figure 21: Depiction of drift time difference versus applied retarding voltage for various RFAs configurations. All the curves have been plotted to have the same maximum potential barrier as the configuration used during the experiment (blue).

5 Conclusion

5.1 Summary

This work focused on the characterization of the open Retarding Field Analyzer in time-of-flight mode. The primary objective was to investigate how varying retarding voltages influence ToF and the accuracy of energy reconstruction for monoenergetic ion beams. Experimental measurements using 5 keV and 7 keV He^+ ion beams were conducted, enabling a direct comparison with simulation results. The data show that energy reconstruction based on ToF in the oRFA aligns closely with simulation predictions. This strong agreement confirms the validity of the simulations in modeling ion behavior within the RFA, opening the possibility of using such simulations to characterize and optimize detector performance. The introduction of deceleration lenses successfully enhanced the ion current at the Faraday cup but also introduced systematic changes in ToF due to beam acceleration. A correction factor was applied to account for this, demonstrating that the lens influence can be quantified and corrected without degrading energy resolution for a monoenergetic beam. Both simulation and experimental results showed consistent ToF responses as a function of retarding voltage, and the observed energy reconstruction trends aligned with theoretical expectations. A key challenge in this study was the determination of the effective ion path length (l), a parameter crucial for accurate energy reconstruction. Since no direct physical measurement was feasible, l was inferred from retarding voltage sweeps, as described in Section 4.3. While this approach yielded reliable and consistent results, an independent and more precise measurement of the ion path length would improve confidence in the analysis. The study also highlighted the advantages of using an oRFA over the traditional gridded configuration. In particular, the oRFA avoids transmission-related issues associated with ion–grid interactions in the gridded RFA. However, it introduces longer drift times as a function of retarding voltage. This trade-off points to the need for further investigation into the oRFA geometry, with the goal of reducing drift time effects without compromising resolution.

5.2 Future Work

A key motivation behind this investigation is the eventual application of the oRFA to characterize and separate ions of different masses and energies, as well as ions of different energies and charges, within a non-monoenergetic beam. Examples of these include EUV-induced hydrogen plasmas and laser-produced tin plasmas, respectively, of which both are present in ASML's nanolithography machines. The ability to resolve time-of-flight signals for each retarding voltage, and reconstruct energy spectra with sufficient accuracy is essential for distinguishing between ion species. The methodology demonstrated here, particularly the use of retarding voltage sweeps combined with precise ToF measurements, forms a foundational basis for this future goal. The accurate mapping of the ion counts or current over ToF for different Vr, as in figure (4) is in principle possible, provided the drift time introduced by the potential of the retarding electrode is small enough to not cause overlapping of closely spaced peaks. The results presented in this work validate simulation results, which can now be incorporated into models to assess if the drift time is sufficiently low to perform energy and mass or charge separated measurements. Moreover, the performance of the oRFA is inherently dependent on its geometry. The distance and position of the grounded electrode relative to the retarding electrode influence the potential distribution within the field region. The length and diameter the retarding electrode also plays a fundamental role. Optimizing these parameters could significantly enhance the drift times values when retarding voltages are active. Hence, experimental observation is called for.

Acknowledgments

The work presented in this thesis would not have been possible without the support and guidance of many people in the Quantum Interactions and Structural Dynamics (QISD) group. First, I would like to sincerely thank Ronnie Hoekstra for giving me the opportunity to carry out this research and for his guidance throughout the project. I am also grateful to Thomas Schlathölter for serving as the second examiner and taking the time to review this thesis. A special thanks goes to Lennart Tinge, not only for providing the essential simulations but also for being a consistently supportive presence throughout the project. I'm also thankful to Mart for his help during the experimental work in the lab. Thanks to Luc, whose enthusiasm during our previous collaboration sparked my interest in this research group. I also want to thank Emiel for his valuable insights during the measurements. To everyone at QISD and ARCNL, thank you for creating such a welcoming and enjoyable environment to work in. Lastly, I am deeply thankful to my family for their constant support throughout these three years of study. Your belief and sacrifices made this journey possible.

Bibliography

[1] L. Chen, W. Wang, and G. Wang, "Electrochemical detection of electrolytes using a solid-state ion-selective electrode of single-piece type membrane," *Biosensors*, vol. 11, no. 4, p. 109, 2021.

[2] C. K. Ober *et al.*, "Recent developments in photoresists for extreme-ultraviolet lithography," *Polymer*, vol. 280, July 2023.

[3] G. McMahon, "Types of ion detector for mass spectrometry," *Technology Networks*, January 2024.

[4] S. Uitjes, "Design of a grid-less retarding field analyser for beams of multiply charged sn ions," July 2023.

[5] C. van Elsberg, "Characterisation of a gridless retarding field analyser," 2024.

[6] L. Assink, "Design analyses for a new experimental rig to study the energy loss of sn ions in h2 gas," 2022.

[7] D. Kucerovsky and Z. Kucerovsky, "Analysis of the dynamic faraday cup," *Journal of Physics D: Applied Physics*, vol. 36, no. 19, p. 2407, 2003. Published 17 September 2003.

[8] L. Tinge, "Charge transfer in low energy sn^{4+} collisions with molecular hydrogen," master's thesis, University of Groningen, Groningen, The Netherlands, July 2024.

[9] D. Verheijde, *Operating Manual: Faraday Cup Transimpedance Amplifier*. Advanced Research Center for Nanolithography (ARCNL), Electronics Engineering Department, Amsterdam, The Netherlands, May 17 2018. Document Version 3.

[10] E. de Wit, "Charge exchange in energetic Sn^{q+}–H_2 collisions," 2023.

Appendices

A 5keV oscilloscope readings

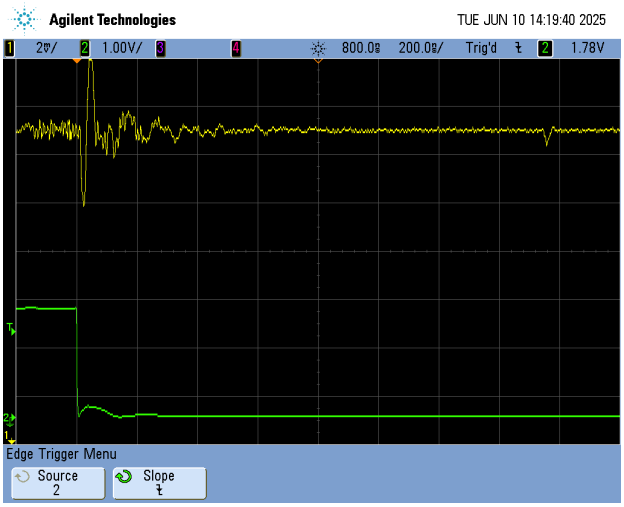

Figure 22: Depicts the oscilloscope readings, for the setup that has inactive deceleration lenses. Where the dip in voltage represents the ions arrival after the chopper action, which triggers at the falling edge of the block pulse (green), for 0V on the retarding electrode.

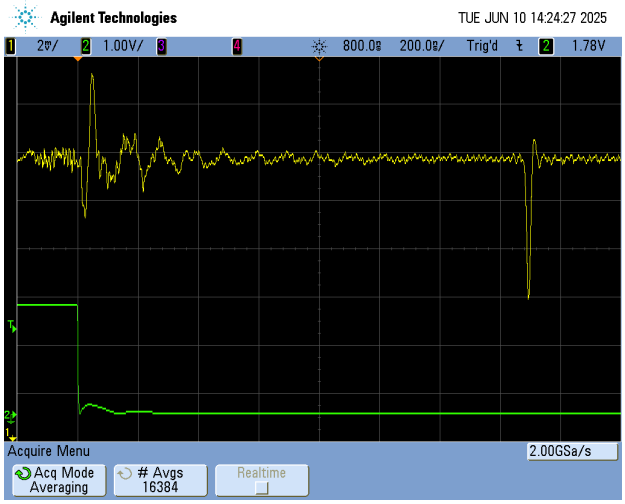

(a) Depicts the oscilloscope readings, for the setup that has active deceleration lenses. Where the dip in voltage represents the ions arrival after the chopper action, which triggers at the falling edge of the block pulse (green), for 0V on the retarding electrode.

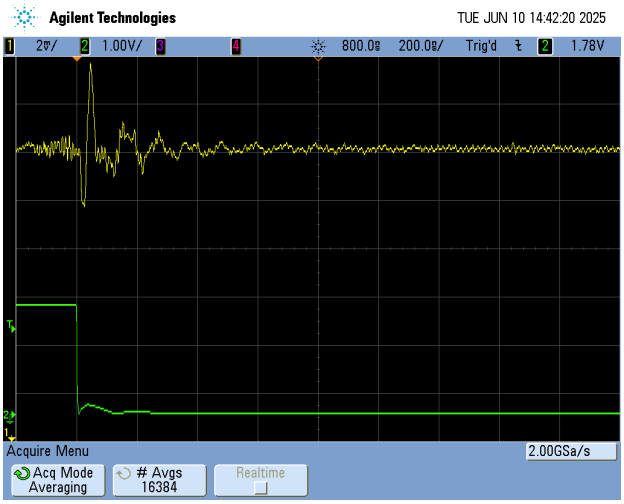

(b) Depicts the oscilloscope readings, for the setup that has active deceleration lenses. Where the dip in voltage represents the ions arrival after the chopper action, which triggers at the falling edge of the block pulse (green), for 5000V on the retarding electrode.

Figure 23: Shows the two configurations of active and inactive deceleration lenses, for a 5keV beam at V_r=0 (right) and V_r=5000 (left).

B 5keV reconstructed energy

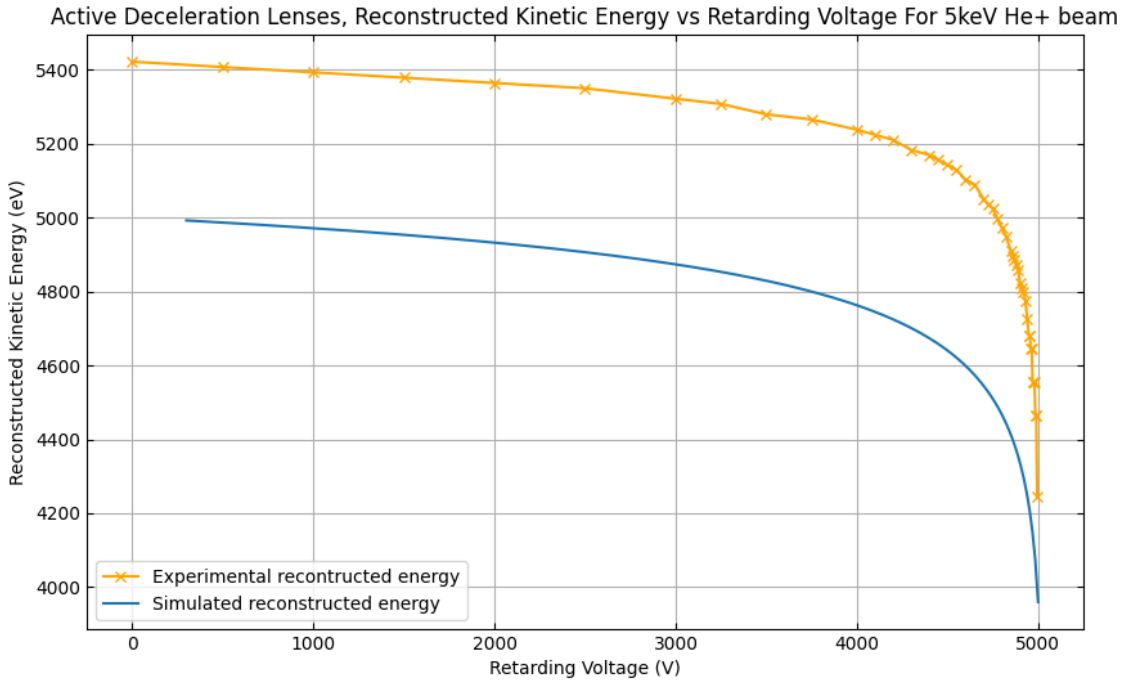

Figure 24: Depicts the reconstructed energy for a range of retarding voltages, compared to the simulation expectation, for the helium beam with 5keV energy, with active deceleration lenses.